Journal of the European Ceramic Society 43 (2023) 6416–6426

Contents lists available at ScienceDirect

Journal of the European Ceramic Society

journal homepage: www.elsevier.com/locate/jeurceramsoc

Spreading and reaction behavior of CMAS-type silicate melts with multiphase Y and Gd aluminate-zirconate T/EBC materials

Eeshani P. Godbole, Nethmi Hewage, David L. Poerschke *

Department of Chemical Engineering and Materials Science, University of Minnesota, USA

ARTICLE INFO

Keywords:
T/EBCs
CMAS
Aluminate
Zirconate
Garnet

ABSTRACT

Thermal and environmental barrier coatings must be robust against attack by calcium magnesium aluminosilicate (CMAS, or CMFAS with iron) deposits, and coatings that produce thin, uniform reaction layers are desirable. The reactions of four multiphase coating compositions in the $AlO_{1.5}$–$REO_{1.5}$–ZrO_2 systems (RE = Gd or Y) with three model CMFAS deposits were studied. Following CMFAS exposure for 1 h at 1400°C, some samples exhibited thin, uniform CMFAS reaction product layers, while others were less uniform with pockets of deep reactions. Coating materials with higher $AlO_{1.5}$ content produced uniform reaction layers, while the most SiO_2-rich CMFAS was most likely to produce a non-uniform response. Apatite was formed in all cases, while the Y was more likely than Gd to form aluminosilicate garnet and cuspidine reaction products. The results are discussed in terms of implications for CMFAS-resistant T/EBC design.

1. Introduction

Jet engines and gas turbines ingest aerosols (sand, ash, dust, and other debris) that can adhere to high-temperature component surfaces, giving rise to deposits composed primarily of calcia, magnesia, alumina, iron oxide, and silica (abbreviated CMAS or CMFAS). Interactions between these deposits and the thermal and environmental barrier coatings (TBCs and EBCs) used to protect metal and ceramic composite components render the coatings vulnerable to thermomechanical damage [1–5]. For TBCs, the damage arises when the initially strain-tolerant coating is stiffened after the melt infiltrates the coating porosity or segmentation features. This increases the cyclic strain energy induced by coefficient of thermal expansion (CTE) mismatch between the coating and alloy. The severity of TBC damage scales with the depth of melt infiltration [3,6–10]. Conversely, for dense, CTE-matched EBCs on ceramic matrix composites (CMCs), the damage is driven by reactions that consume the coating and produce a phase assemblage with increased CTE mismatch. The severity of EBC damage is dictated by the overall depth of reactive consumption and the thermophysical properties of the reaction products [3,7,11,12].

Most approaches to mitigate deposit-induced coating degradation focus on controlling the reactions between the coating and melt. For TBCs, one objective is to promote rapid reactive crystallization to block melt infiltration pathways, thereby limiting the stiffened depth. For rare earth (RE) containing TBC materials, the fast-nucleating Ca-RE silicate apatite reaction product is preferred, although a variety of other reaction products (e.g., RE-containing silicates such as garnets, cyclosilicates, or cuspidine) can also provide benefits by consuming the melt. For EBCs, the objectives are to either (i) minimize reactivity (and thus the reactive consumption of the coating), (ii) form dense reaction product layers that slow coating dissolution, or (iii) avoid CTE-mismatched reaction products. These reaction-based mitigation approaches are expected to be less effective at higher operating temperatures due to increased reaction rates and reduced driving force for crystallization reactions due to expanding melt fields.

The nature of the melt spreading on a surface relative to infiltration or inward reaction with the coating material impacts the severity of the deposit-induced degradation [13–17]. In this article, the term spreading is used to encompass all aspects of lateral redistribution including wetting of the coating material, reactive wetting, and the effects of melt viscosity on gravity-driven flow across the surface. Based on the relevant surface energies, it is expected that the silicate melts will wet the typical oxide coating materials [17–20]. This is consistent with observations that the melts wick into pores and intercolumnar gaps in coatings. Other observations suggest that due to the combination of surface microstructure (e.g., nanostructured column tips in EB-PVD coatings), surface energies, and gas flow dynamics the melt can initially bead up or partially dewet and move around the coating surface before infiltration

* Corresponding author.
E-mail address: dpoersch@umn.edu (D.L. Poerschke).

https://doi.org/10.1016/j.jeurceramsoc.2023.05.046
Received 28 February 2023; Received in revised form 6 May 2023; Accepted 28 May 2023
Available online 31 May 2023
0955-2219/© 2023 Elsevier Ltd. All rights reserved.

and reactions occur [13,15,20]. Surface microstructure engineering to promote dewetting (and subsequent removal of molten droplets facilitated by the high gas velocity) has been proposed as a potential mitigation strategy [21–23]. However, Fig. 1(a,b) illustrates a potential disadvantage of this behavior. If a solid, adhered deposit melts during a higher temperature excursion, partially dewets, and then begins infiltrating or reactively wetting the surface, the melt would be concentrated in specific areas. Although a smaller coating area would experience deposit-induced distress, the higher local deposit concentration could increase the infiltration or reaction depths and the likelihood for deep cracking or other severe coating damage.

Conversely, in cases where the melt spreads laterally faster than it infiltrates or dissolves the coating, a larger coating area would be exposed to the deposit but there would be a thinner, more uniform infiltration or dissolution-reprecipitation reaction layer (Fig. 1(c)). The thin stiffened layer is also more likely to induce exfoliation-type cracking, removing the surface deposit and a thin layer of the coating, while leaving most of the coating intact. Identifying coating materials that promote the uniform spreading and reaction of molten silicate deposits could improve coating durability. This approach could be adapted for the entire coating architecture or be incorporated as a highly reactive top coat acting as a sacrificial layer [3,6,15,16,24].

Achieving the response illustrated in Fig. 1(c) requires coatings that (i) efficiently convert the melt to crystalline reaction products with minimal coating dissolution, (ii) promote reactive wetting of the melt, and (iii) produce similar response to a variety of silicate deposit compositions. There is a growing body of knowledge about CMFAS-coating reactions, but less attention has been devoted to understanding reactive wetting and melt spreading. The dynamics of wetting, spreading, and infiltration depend on various temperature- and composition-dependent properties including the surface tension and viscosity of the melt, the coating material surface energy, and the coating surface microstructure [14,15,22–27]. The nature and extent of the melt spreading is further influenced by reactions with the coating, including dissolution into the melt, melt infiltration into the coating microstructure, and the formation of reactive crystallization products that could promote reactive wetting [24,28]. Some studies have analyzed the initial wetting and spreading behavior of certain deposits [17,24,29] on specific coating materials. In some CMFAS exposure tests with rare earth monosilicates and disilicates, lower-viscosity CMFAS melts gathered towards the center with a dome-like appearance while higher-viscosity CMFAS melt retained a flatter appearance in the original area of application. In both cases, the reaction region appeared localized to the area where the deposit was applied, with minimal spreading [30,31]. These observations demonstrate the variations in CMFAS melt spreading based on the inherent CMFAS properties and the influence of reactions.

With this background, this study is motivated by two objectives:

1. To test the hypothesis that multiphase coating materials based on combinations of RE zirconates and aluminates could produce a more uniform reaction response to a broad range of CMFAS compositions compared to single-phase binary compounds.
2. To develop and evaluate new methods to quantify the reaction depth and spreading to facilitate better direct comparisons between the performance of various coating materials in efficient pellet-based tests, while generating quantitative data features to facilitate future data-driven materials discovery efforts.

The novelty of the material design approach lies in engineering coating materials to limit silicate melt infiltration by redistributing the melt to form thin, uniform reaction layers. These materials could also meet or balance other requisite thermophysical and thermochemical properties. In these materials, the zirconate (or a ZrO_2-containing rare earth oxide) is expected to contribute to low thermal conductivity while the aluminates could promote beneficial reactivity with CMFAS. The addition of the aluminate also lowers the coefficient of thermal expansion (CTE) of the composite relative to a pure zirconate or equivalent hafnate [32–38], making these materials more amenable as top coats for multilayer T/EBCs that have been proposed for use on CMCs or refractory alloys [39–41]. Finally, some aluminate-zirconate composites exhibit higher toughness [32,42].

Four coating material compositions (Fig. 2) with constant 85RE:15Zr molar ratio were selected to study the effect of the alumina content (either 10 mol% or 30 mol% $AlO_{1.5}$) and RE identity (either Y or Gd) on the reactions with CMFAS. The low-$AlO_{1.5}$ stoichiometry ($A_{10}RE_{76}Z_{14}$)* falls in the phase field containing the cubic RE oxide (c-$REO_{1.5}$), fluorite (F), and rare earth aluminate monoclinic phase ($RE_4Al_2O_9$, YAM or GdAM). The high-$AlO_{1.5}$ stoichiometry ($A_{30}RE_{60}Z_{10}$) falls in phase field containing the rare earth aluminate perovskite, ($REAlO_3$, YAP or GdAP) in equilibrium with F and (Y/Gd)AM. Coupons exposed to one of three model CMFAS compositions for 1 h at 1400°C were characterized to identify reaction products and the depth and lateral spread of the reaction process. This article focuses on observations related to presence of specific reaction products, melt consumption, reaction depth, and spreading to understand if specific reaction pathways facilitate attaining thin, uniform reaction layers across multiple CMFAS compositions. Additional details about the reaction product compositions and reaction pathways are reported separately [44].

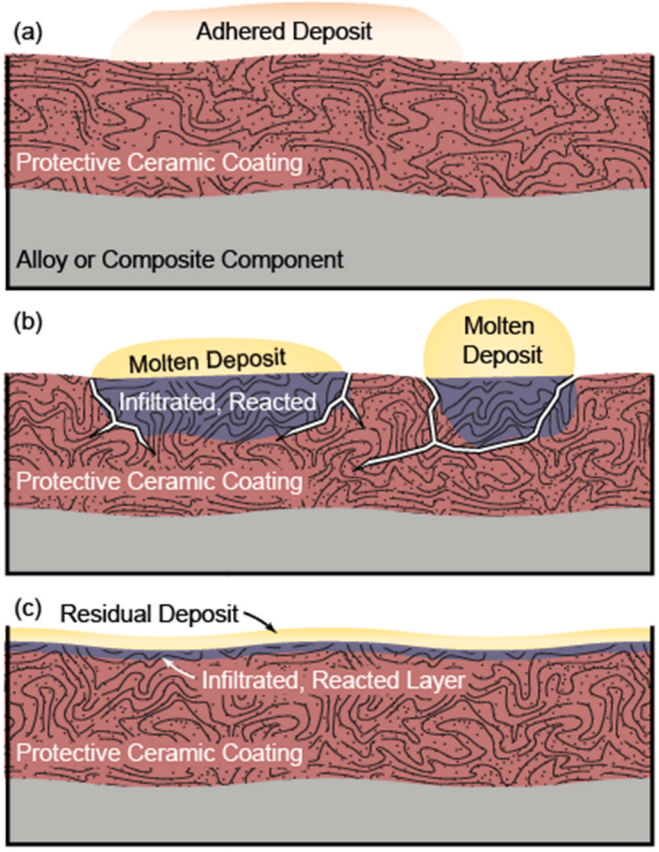

Fig. 1. Upon melting, an (a) adhered solid CMFAS deposit could either (b) partially de-wet leading to localized deeper infiltration and reaction layer or (c) spread across the coating surface faster than it infiltrates or reacts, leading to a thinner CMFAS-affected layer.

* All coating material and CMFAS deposit composition are abbreviated as mole percentages of the single-cation oxide formulae, abbreviated to integer values using the first letter of the cation symbol, e.g., $A_{30}G_{60}Z_{10}$ is 30 mol% $AlO_{1.5}$, 59.5 mol% $GdO_{1.5}$ and 10.5 mol% ZrO_2.

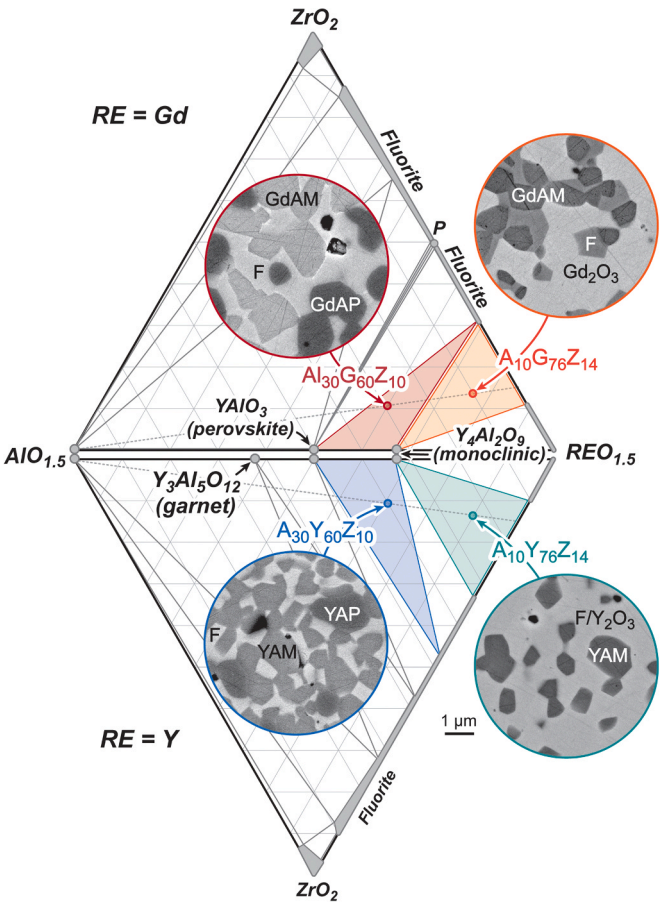

Fig. 2. The coating material compositions studied are plotted on 1500 °C isothermal $AlO_{1.5}$-$REO_{1.5}$-ZrO_2 ternary diagrams calculated with the Thermo-Calc TCOX10 database. Inset micrographs show the microstructures of the test coupons after sintering at 1500 °C for 50 h.
Adapted from [43].

2. Experimental methods

2.1. Material preparation

2.1.1. Candidate coating materials

The mixed aluminate-zirconate materials were synthesized by reverse-coprecipitation using calibrated precursor solutions mixed to yield the desired stoichiometries and then added dropwise to an ammonium hydroxide (28–30 % Sigma Aldrich) solution maintained at pH > 10. Saturated solutions of gadolinium, yttrium, and aluminum nitrates (Alfa Aesar (AA), Ward Hill, MA, purity > 99.9 % metal basis) in 200 proof ethanol and zirconium nitrate (AA, purity > 99.9 % on a metal basis) in distilled water were used as precursors. The precipitates were washed with 200 proof ethanol, dried at 70 ℃, ground using an alumina mortar and pestle, and pyrolyzed at 1000 ℃. The pyrolyzed powders were then ball milled for 4 h at 25 Hz in zirconia jars using zirconia milling media with 200 proof ethanol as a dispersing medium, dried, and uniaxially cold pressed into 13 mm diameter pellets weighing approximately 250 mg. These pellets were sintered in platinum cups in covered alumina crucibles at 1500 ℃ for 50 h with a heating rate of 2 ℃/min and a cooling rate of 10 ℃/min.

2.1.2. CMFAS powders

Three model CMFAS deposits compositions were used to investigate the effect of the Ca:Si ratio and the total Mg^{2+}, $Fe^{2+/3+}$ and Al^{3+} ($\sum MFA$) content. The $C_{10}M_5F_5A_{10}S_{70}$ and $C_{31}M_9F_5A_{12}S_{43}$ deposits are based on those used by Summers to study the effect of the Ca:Si ratio on reactions with EBC materials [30,31]. The $C_{15}M_{12}F_{12}A_{16}S_{45}$ composition, which has an intermediate Ca:Si ratio, was designed to test higher $\sum MFA$ content [45]. Calcia (CaO 99.95 % pure, AA), magnesia (MgO 98 %, Acros Organics, Morris Hill, NJ), alumina ($AlO_{1.5}$ 99.95 %, AA), and silica (SiO_2 99 %, AA) were calcined at 1100 °C, and mixed with iron(III) oxide (99.9 %, AA) in the desired stoichiometries. The mixtures were ball milled at 40 Hz for 20 min using alumina jars and milling media with 200 proof ethanol as a dispersing medium, dried, and pre-reacted for 24 h at either 1000 °C or 1100 °C, depending on the incipient melting temperature.

2.2. CMFAS exposure experiments

The sintered aluminate-zirconate coupons were flattened using SiC papers and polished to a 1 µm finish using diamond lapping films. The CMFAS powders were applied to the center of the polished pellet surface by sieving through a 4 mm diameter stencil to achieve a 15 mg/cm^2 areal loading. The samples were placed in platinum cups in covered alumina crucibles, heated to 1300 ℃ at 20 ℃/min, then from 1300 ℃ to 1400 ℃ at 10 ℃/min, held for 1 h, and step-cooled to room temperature.

2.3. Characterization

The CMFAS-exposed coupons were mounted in epoxy, cross-sectioned, remounted, and polished using diamond suspensions to a 1 µm finish. The samples were characterized with backscattered scanning electron microscopy (BS-SEM, Hitachi SU8230). Micrographs were recorded across the entire coupon cross section at sufficient magnification to capture details of the reaction layer and the interface with unreacted material. Quantitative chemical analyses of the reaction products formed were performed using electron probe microanalysis with wavelength dispersive spectroscopy (EPMA-WDS, JEOL JXA-8530FPlus). Data acquisition was done using a focused beam diameter 15 kV accelerating voltage and 30 nA beam current. Details about the detector assignments and standards are reported elsewhere [44,46,47]. Phases were identified using a combination of morphology, BSE contrast, and composition using knowledge about the relevant phases from prior studies [46–49].

3. Results and discussion

3.1. As-synthesized materials

Fig. 2 shows micrographs of polished cross sections of the starting materials after sintering for 50 h at 1500°C. The phase assemblages were consistent with those expected based on the isothermal phase diagrams. Analysis of polished cross section microstructures showed that the sintered pellets contained less than 5 % porosity with grain sizes of order several micrometers. The relative density is high enough that infiltration of interconnected porosity is not expected and was not observed. The small grain size and uniform distribution of the phases means that the reaction response is expected to be uniform across the surface of the samples.

3.2. Macroscopic observations of test coupons after CMFAS exposure

Fig. 3 shows photographs of the sample surfaces after CMFAS exposure revealing varying degrees of lateral spread of the molten deposits with the final perimeter ranging from roughly the original area of deposit application to nearly reaching the edges of the pellets. The overall degree of spreading is tabulated in Table 1 as a percentage increase from the initial area of the applied deposit. In most cases, the CMFAS spreading is radially symmetric. Some of the reaction areas showed two distinct regions with a central darker region and a lighter periphery, suggesting a thicker reaction layer near the center. Upon

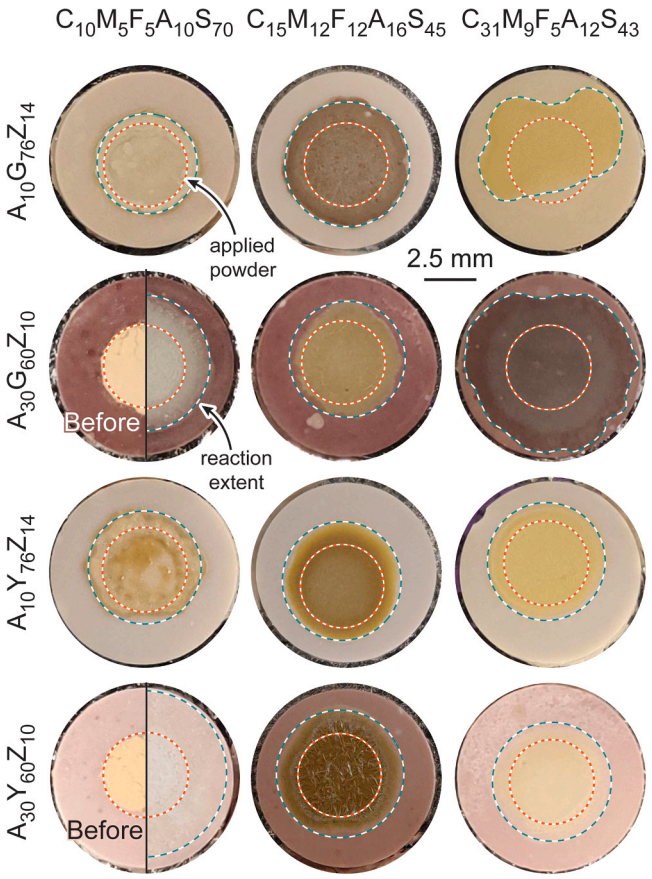

Fig. 3. Photos of the test coupons after 1 h, 1400 °C CMFAS exposures. Two examples of the appearance before the experiment are overlaid for comparison.

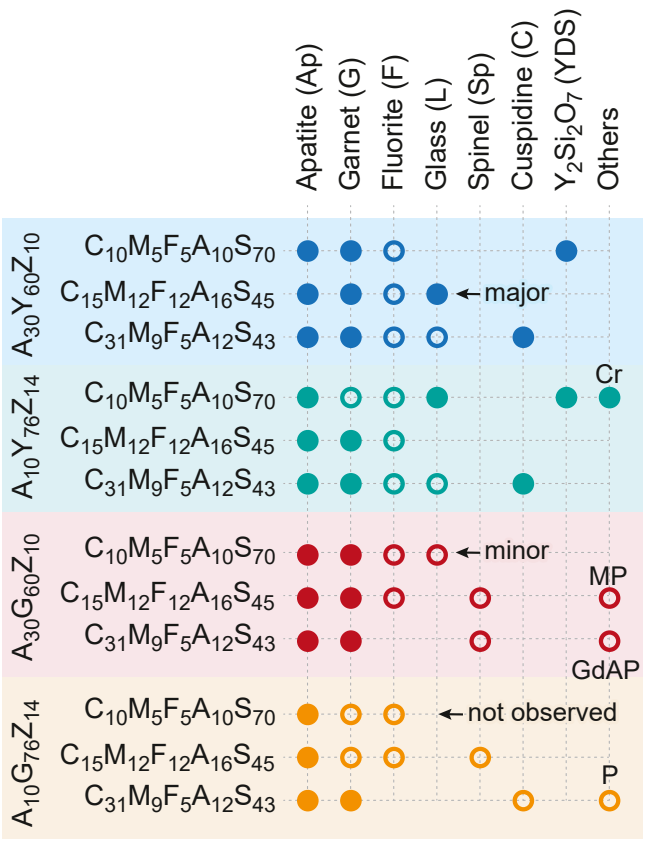

Fig. 4. Prevalence of specific reaction products in the reaction layer for each sample. Major is defined as > 25% area fraction in the reaction layer cross section.

Table 1
Percentage increase in area after the CMFAS exposure.

CMFAS composition → Coating material ↓	$C_{10}M_5F_5A_{10}S_{70}$	$C_{15}M_{12}F_{12}A_{16}S_{45}$	$C_{31}M_9F_5A_{12}S_{43}$
$A_{10}G_{76}Z_{14}$	38 %	116 %	116 %
$A_{30}G_{60}Z_{10}$	141 %	58 %	314 %
$A_{10}Y_{76}Z_{14}$	95 %	83 %	95 %
$A_{30}Y_{60}Z_{10}$	307 %	121 %	102 %

reaction with the Ca lean $C_{10}M_5F_5A_{10}S_{70}$ deposit, the $AlO_{1.5}$-lean $A_{10}G_{76}Z_{14}$ and $A_{10}Y_{76}Z_{14}$ samples exhibited a thick ridge of reaction products around the perimeter of the original deposit location with a varied distribution of reaction products towards the center. A generally uniform CMFAS spreading behavior in each test coupon (except for $A_{10}G_{76}Z_{14}$-$C_{31}M_9F_5A_{12}S_{43}$) implies that cross-sections taken through the center of the test coupons should be representative of the overall reaction layer in each test coupon.

3.3. Reaction product identification

A variety of reaction products were observed, and the reaction layer for some coupons contained residual melt. Details about the analysis and trends in the reaction product identification and composition are provided elsewhere [44]. This section summarizes key results from [44] that are relevant for the subsequent discussion. The prevalence of each reaction product is illustrated in Fig. 4. The apatite composition was typically close to $Ca_2RE_8(SiO_4)_6O_2$, with minor solubility of Mg, Zr, Al, Fe ions. The compositions of the garnet phase, which can be represented as $RE_3Al_2Al_3O_{12}$ to represent two different coordination numbers for Al [46,47], varied more significantly. The garnets formed with the Y-based samples had silicon substituting for between one-third and one-half of the alumina in the three tetrahedral aluminum sites. The mechanism of coupled substitution of Ca^{2+}, Mg^{2+}, and Si^{4+} for Y^{3+} and Al^{3+} in YAG is well documented at 1400 °C, even in the absence of $Fe^{2+/3+}$ and Zr^{4+} [46]. Conversely, the garnets formed by reactions in the Gd-based systems were closer to the pure aluminate endmember $Gd_3Al_5O_{12}$. This is result is consistent with the fact that Gd containing garnets do not form at equilibrium at 1400 °C in the Gd + CMAS system [47]. Instead, it appeared that $Fe^{2+/3+}$ and Zr^{4+} substitutions for Al^{3+}, with charge compensating Ca^{2+} and Mg^{2+} substitutions play a more important role in stabilizing the garnet here. The ZrO_2-based fluorite phase typically contained between 25 mol% and 35 mol% $REO_{1.5}$, corresponding to a depletion of between half and two thirds of the RE present in the initial fluorite. A Mg- and Fe-rich spinel phase (Sp), magnetoplumbite (MP, $REAl_{11}O_{18}$ with some solubility of Ca, Mg, Zr, and Fe ions), periclase (P, MgO), and cuspidine (Ca and Si substitution for RE and Al in $RE_4Al_2O_9$ as reported in [37,50–54] appeared as minor phases in the reaction layers formed for one or more Gd-containing systems. $Y_2Si_2O_7$ (YDS) and cuspidine (C) appeared as major reaction products in the two Y-containing samples exposed to the Si-rich $C_{10}M_5F_5A_{10}S_{70}$ and Ca-rich $C_{31}M_9F_5A_{12}S_{43}$ deposits, respectively. Minor quantities of cristobalite (Cr, SiO_2) were also observed in several cases.

3.4. Analysis of reaction layer profiles

3.4.1. Feature identification and quantification approach

Fig. 5(a) shows a stitched cross-section micrograph of the CMFAS reaction zone for the $A_{30}G_{60}Z_{10}$ – $C_{10}M_5F_5A_{10}S_{70}$ sample. The reaction layer under the initial deposit position extends approximately 100 μm below and only slightly (up to 25 μm) above the original sample surface. After accounting for the porosity in the reaction layer, the implication is

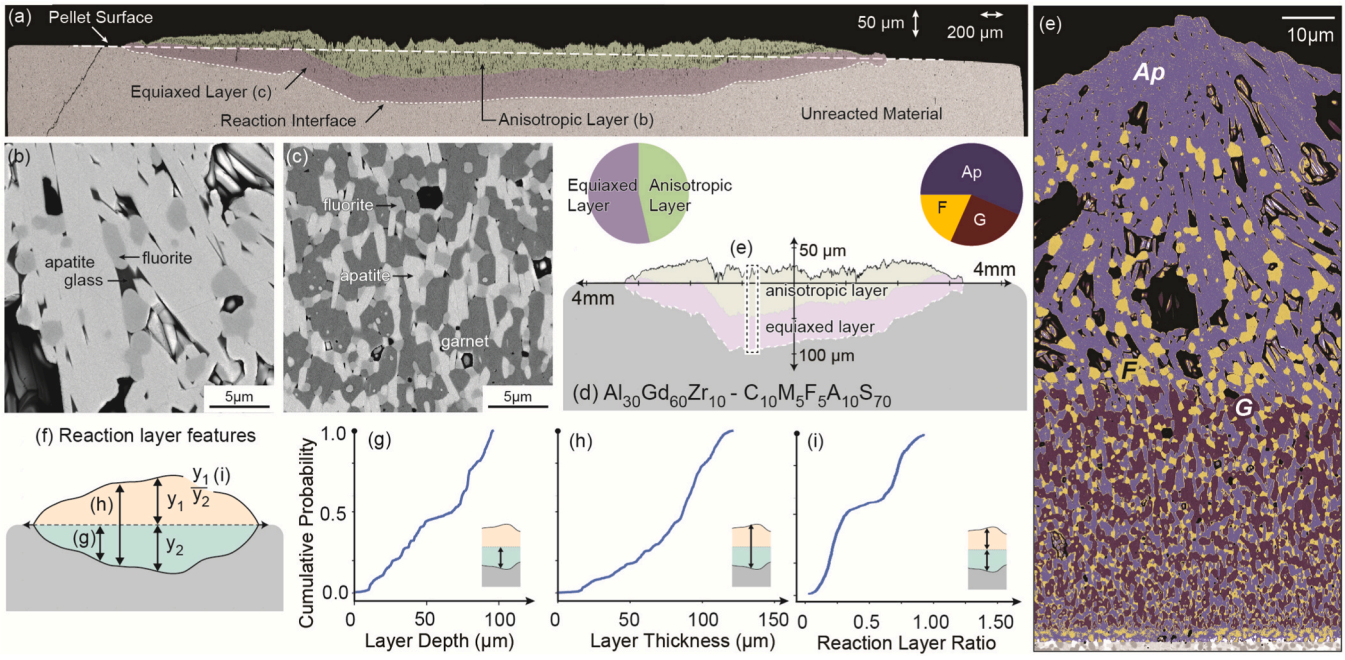

Fig. 5. (a) Cross section of the $A_{30}G_{60}Z_{10}$ – $C_{10}M_5F_5A_{10}S_{70}$ sample showing the anisotropic (green, enlarged in (b)) and equiaxed (purple, enlarged in (c)) reaction zones. (d) Reaction layer profile based on layers in (a). (e) False colored BSE micrograph showing the distribution of apatite, garnet, and fluorite. The areal distribution of the anisotropic layer and the equiaxed layer and the primary reaction product phase fractions are shown as pie charts. Cumulative probability distributions (CPD) for the (g) reaction layer depth below the original surface, (h) reaction layer thickness, and (i) ratio of the reaction layer thickness above and below the original pellet surface.

that the initial reactions likely do not significantly increase the volume of crystalline phases relative to the volume of material dissolved. The reaction layer becomes progressively thinner toward the edges, and a greater proportion of this layer is above the initial pellet surface. This could suggest that the crystallization efficiency increases once the initial dissolution reactions saturate the melt with RE, Zr, and Al oxides.

The reaction layer shows two distinct morphologies. An *anisotropic layer* has larger, faceted grains that likely grew in presence of significant melt, and more porosity (e.g., Fig. 5(b)) while the *equiaxed layer* has smaller, equiaxed grains that likely formed in the presence of less melt (e.g., Fig. 5(c)). Here the transition between the anisotropic and equiaxed layers is abrupt, while in other samples had a *transition layer* with intermediate grain sizes and morphologies. The relative ratios of each of the anisotropic and equiaxed layers are shown as a pie chart in Fig. 5.

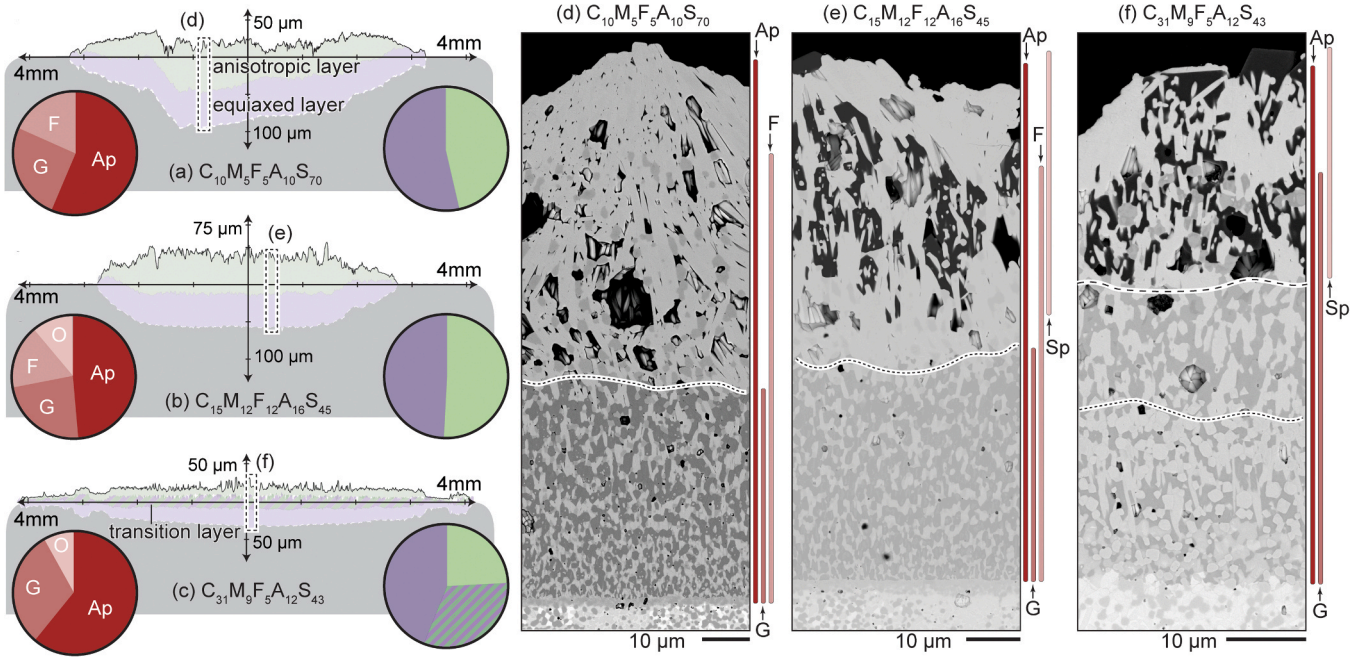

Fig. 6. (a-c) Reaction product profiles for $A_{30}G_{60}Z_{10}$ samples. Pie charts show (left) the fraction of the predominant reaction products (O = others) and (right) the area fraction of the reaction morphology zones. (d-f) Representative reaction layer microstructures. White dashed lines delineate the different reaction morphology zones.

Variations in the equiaxed reaction layer thickness across samples could be due to variations in rates of melt consumption by the crystalline products which form in the initial reaction stages.

The boundaries of the reaction layer and between morphology zones were recorded every 10 μm across the cross section. These values were used to plot the reaction profile in Fig. 5(d), and subsequent analysis. The relative phase fractions of each crystalline phase estimated for a representative region of the thickest reaction layer (Fig. 5(e)) are shown in the adjacent pie chart. The features illustrated in Fig. 5(f) are plotted as cumulative probability distributions (CPD) to compactly capture the magnitude and variation in each value. These features include the Fig. 5 (g) reaction layer depth below the original pellet surface, Fig. 5(h) total reaction layer thickness from the outer surface of the reaction layer to the reaction front, and Fig. 5(i) the ratio of the portions of the reaction layer that are located above and below the original pellet surface. Similar analysis for each sample is described in the following sections.

3.4.2. $A_{30}G_{60}Z_{10}$ observations

Fig. 6(a-c) shows plots of the cross-section reaction layer profiles formed when $A_{30}G_{60}Z_{10}$ is exposed to the three deposits. Pie charts show the relative phase fractions of key phases and the contributions of each reaction zone type. Fig. 6(d-f) show micrographs of thicker regions of each reaction layer; the adjacent colored bars show the approximate spatial distribution of the crystalline reaction products [44]. The reaction layer formed on exposure to $C_{31}M_9F_5A_{12}S_{43}$ is the thinnest and shows the greatest spread. It also showed a more gradual change in reaction product morphology through its thickness with a significant transition layer. The reaction layers on the $C_{10}M_5F_5A_{10}S_{70}$ and $C_{15}M_{12}F_{12}A_{16}S_{45}$ samples were thicker and have similar thicknesses of the anisotropic and equiaxed layers. However, while most the reaction layer on the $C_{10}M_5F_5A_{10}S_{70}$ sample was below the original pellet surface, that on $C_{15}M_{12}F_{12}A_{16}S_{45}$ is more equally distributed above and below the original pellet surface.

Apatite and garnet formed in all three tests. Apatite predominates, comprising roughly half or more of the reaction product volume and appearing through the entire reaction layer thickness. For the $C_{10}M_5F_5A_{10}S_{70}$ and $C_{15}M_{12}F_{12}A_{16}S_{45}$ samples, garnet appears mid-way through the thickness and its appearance is coincident with the anisotropic-to-equiaxed transition. For $C_{31}M_9F_5A_{12}S_{43}$, garnet appears much closer to the top surface and is present through the anisotropic, transition, and equiaxed layers. Spinel is intermixed with apatite and toward the top of the reaction layer formed by $C_{15}M_{12}F_{12}A_{16}S_{45}$ and $C_{31}M_9F_5A_{12}S_{43}$, suggesting that these phases precipitate earlier in the reaction for deposits containing a higher proportion of Mg and Fe. The anisotropic morphologies could suggest that they formed surrounded by melt, giving flexibility to take on an energetically favorable crystallite shape. Fluorite appears upon exposure to the $C_{10}M_5F_5A_{10}S_{70}$ and $C_{15}M_{12}F_{12}A_{16}S_{45}$ deposits but not $C_{31}M_9F_5A_{12}S_{43}$, where more ZrO_2 is incorporated into the garnet. The reaction layers showed largely the same phases with only variations in phase fractions towards the center and periphery, except that those reactions with $C_{10}M_5F_5A_{10}S_{70}$ formed magnetoplumbite near the periphery.

3.4.3. $A_{10}G_{76}Z_{14}$ observations

Fig. 7 shows observations of reaction layers formed when the $AlO_{1.5}$-lean $A_{10}G_{76}Z_{14}$ coating material was exposed to the three CMFAS deposits. Fig. 7(a) shows that the $C_{10}M_5F_5A_{10}S_{70}$ exposure produced significant lateral variation in the reaction depth and intensity. A thick, deep reaction layer coincides with the raised ridges observed in Fig. 3 around the periphery of the CMFAS deposit while the reaction layer towards the center is thinner and partially recessed below the original pellet surface. One explanation could be that the melt began to uniformly dissolve the pellet before partially dewetting (similar to schematic shown in Fig. 1(b)) leading to significant reaction product

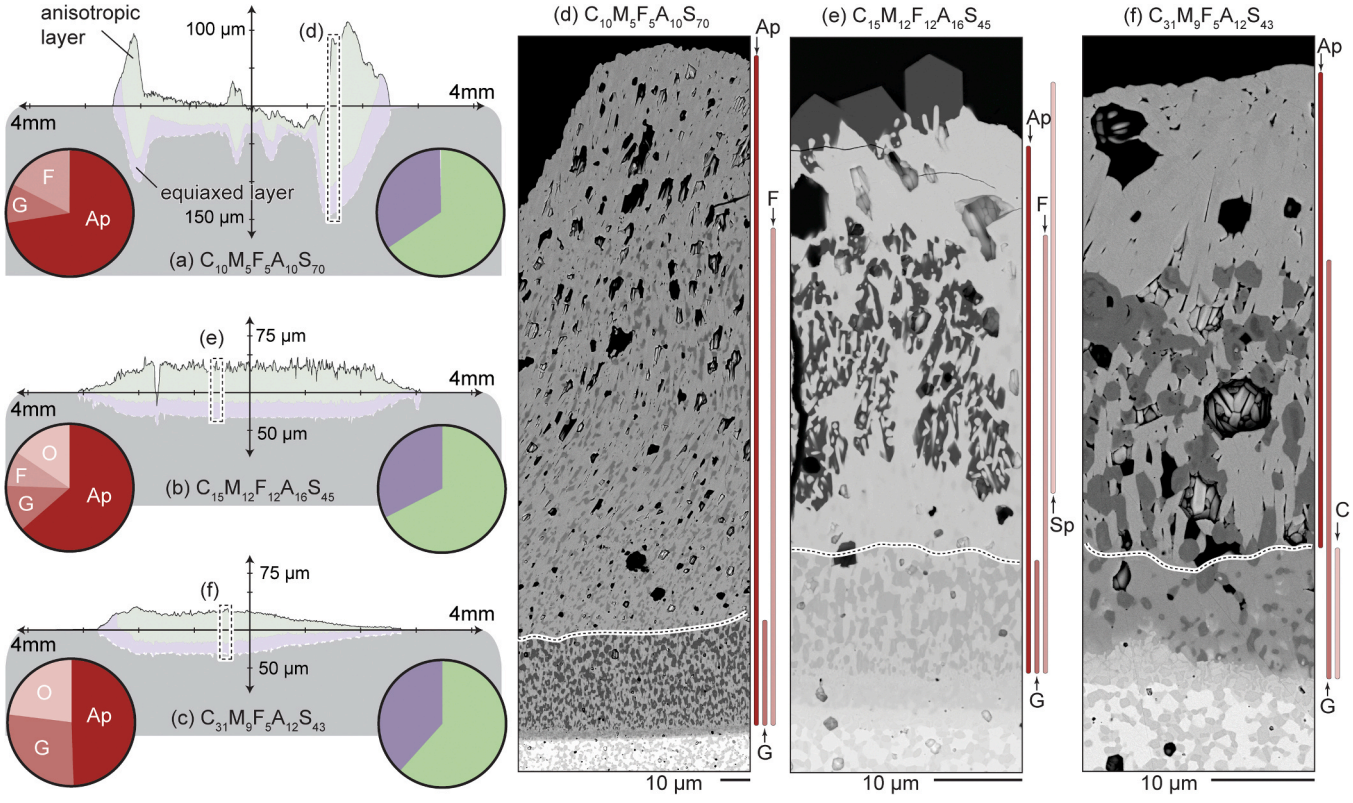

Fig. 7. (a-c) Reaction layer profiles for the $A_{10}G_{76}Z_{14}$ samples exposed to the three model CMFAS deposits. Pie charts show the areal distribution of (left) the reaction products and (right) the three reaction morphology zones. (d-f) Micrographs showing representative portions of the reaction layer cross section, where white dashed lines delineate the different morphology zones.

accumulation in areas where the melt was concentrated. This behavior could be driven by changes in melt surface energy or viscosity during the initial reaction, but there is currently insufficient data on these dynamics to draw a definite conclusion. On the other hand, Fig. 7(b,c) show that the reactions with $C_{15}M_{12}F_{12}A_{16}S_{45}$ and $C_{31}M_9F_5A_{12}S_{43}$ produce a fairly uniform reaction layer thicknesses. The extent of lateral CMFAS spread is similar amongst the three coupons.

The micrographs in Fig. 7(d-f) show that apatite is again the predominant reaction product, and that it (along with spinel for $C_{15}M_{12}F_{12}A_{16}S_{45}$) appears first in the reaction layer. Garnet is also observed for all three cases. For $C_{10}M_5F_5A_{10}S_{70}$ and $C_{15}M_{12}F_{12}A_{16}S_{45}$ garnet only forms in the thin equiaxed zone near the bottom of the reaction layer. For $C_{31}M_9F_5A_{12}S_{43}$, garnet appears primarily mixed with apatite in the central region of the reaction layer under the surface layer of apatite, and is a minor phase in the equiaxed inner layer, which is composed primarily of cuspidine. As with the $A_{30}G_{60}Z_{10}$ material, fluorite is present throughout much of the reaction layer formed with $C_{10}M_5F_5A_{10}S_{70}$ and $C_{15}M_{12}F_{12}A_{16}S_{45}$ but not $C_{31}M_9F_5A_{12}S_{43}$. Spinel appears as a major reaction product with the $C_{15}M_{12}F_{12}A_{16}S_{45}$ deposit. Occasional periclase grains were observed in the $C_{31}M_9F_5A_{12}S_{43}$ sample. Despite the known importance of high Ca:Si ratio to drive apatite-forming reactions in some T/EBC materials, these results show decreasing apatite fraction as the Ca:Si ratio in the deposit is increased.

3.4.4. $A_{30}Y_{60}Z_{10}$ observations

Fig. 8(a-c) shows the reaction layers for the $A_{30}Y_{60}Z_{10}$ samples with pie charts illustrating the reaction zone morphology and phase fractions based on the sections shown in Fig. 8(d-g). The extent of lateral melt spreading increases moving from an exposure to Ca-rich $C_{31}M_9F_5A_{12}S_{43}$ to the Ca-lean $C_{10}M_5F_5A_{10}S_{70}$ deposit. The $C_{10}M_5F_5A_{10}S_{70}$ and $C_{15}M_{12}F_{12}A_{16}S_{45}$ reaction layer profiles show a "dipped" appearance in the center attributed to less efficient melt consumption by the reactions occurring initially under the deposit compared to those as the RE- and Zr-saturated melt spread outward.

Apatite is a major reaction product present through most or all of the reaction layer thickness for each sample. The central region of the $C_{15}M_{12}F_{12}A_{16}S_{45}$ sample had loosely adhered apatite grains measuring several tens of microns across and a few hundred microns long, which are visible in Fig. 3. The near-surface regions of the $C_{31}M_9F_5A_{12}S_{43}$ sample are also primarily apatite, albeit with much smaller grains. Conversely, the surface of the center of the sample exposed to $C_{10}M_5F_5A_{10}S_{70}$ is decorated with large YDS grains, which become less prevalent (replaced by finer apatite grains) moving outward toward the edges of the reaction zone. Below the surface, all three reaction layers transition to a mixture of apatite, garnet, and fluorite, which are observed through the transition and equiaxed zones. Cuspidine appears only toward the bottom of the reaction layer for the Ca-rich $C_{31}M_9F_5A_{12}S_{43}$ deposit. The pie charts in Fig. 8(a-c) show that the fraction of apatite and fluorite formed decrease relative to the garnet and cuspidine aluminosilicates as the Ca:Si ratio in the deposit increases from $C_{10}M_5F_5A_{10}S_{70}$ to $C_{31}M_9F_5A_{12}S_{43}$. This observation supports the hypothesis from earlier phase equilibria studies that even with a high Ca:Si ratio, systems rich in alumina (derived here from dissolution of the coating material) will drive crystallization of garnet rather than apatite.

3.4.5. $A_{10}Y_{76}Z_{14}$ observations

The reaction profiles for the $A_{10}Y_{76}Z_{14}$ samples (Fig. 9(a-c)) show similar lateral spreading but notable differences in the reaction product microstructures and identities. Fig. 9(b,c) shows that $C_{15}M_{12}F_{12}A_{16}S_{45}$ and $C_{31}M_9F_5A_{12}S_{43}$ produced relatively uniform reaction layers while $C_{10}M_5F_5A_{10}S_{70}$ produced a thicker reaction layer towards the periphery corresponding to the ridge-like outer ring shown in Fig. 3.

Fig. 9(d,e) shows the inhomogeneity in reaction products produced by reaction with $C_{10}M_5F_5A_{10}S_{70}$. This sample showed the highest retained melt volume present with cristobalite in reservoirs inside the crystalline ring around the periphery. Despite the presence of melt through most of the reaction layer, the thin equiaxed layer appears to protect against continued dissolution of the pellet. YDS appears throughout the entire reaction layer, while for $A_{30}Y_{60}Z_{10}$ the YDS grains were localized towards the center of the reaction zone. Fig. 9(f,g) shows that for $C_{15}M_{12}F_{12}A_{16}S_{45}$ and $C_{31}M_9F_5A_{12}S_{43}$ the initial surface layer comprised primarily of apatite quickly transitions to a mixture of apatite, garnet, and fluorite. For $C_{15}M_{12}F_{12}A_{16}S_{45}$ this assemblage continues through the entire reaction layer thickness, with gradually reducing grain size. For $C_{31}M_9F_5A_{12}S_{43}$ a thin layer of mixed apatite, garnet, and fluorite transitions to a layer of mostly anisotropic garnet

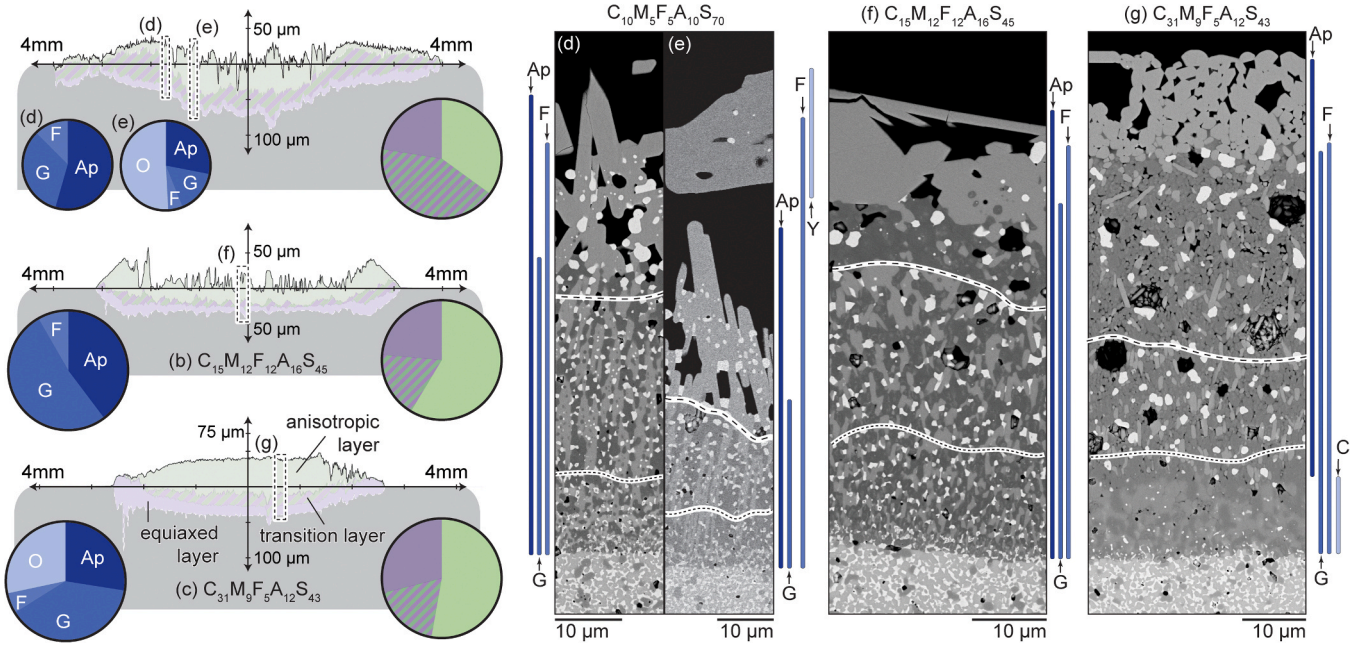

Fig. 8. (a-c) Reaction profiles for $A_{30}Y_{60}Z_{10}$ samples exposed to the three model CMFAS compositions. Pie charts show the areal distribution of the key crystalline reaction product (left, O = all others) and the three reaction zones morphologies (right). (d-g) BSE micrographs showing a magnified cross section of the reaction layer in each test coupon with dashed lines delineate the morphology zones.

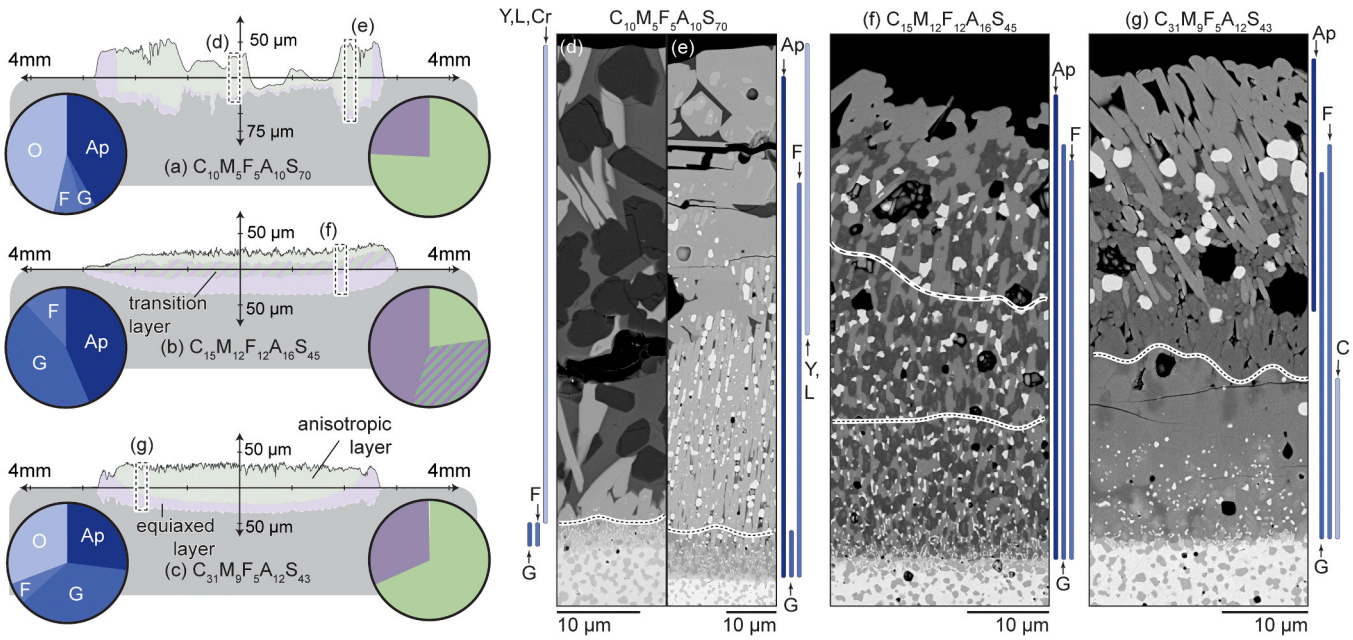

Fig. 9. (a-c) Reaction profiles for the $A_{10}Y_{76}Z_{14}$ samples exposed to the three CMFAS compositions. Pie charts to the left and right of each reaction profile show the areal distribution of phases and morphology zones, respectively. (d-g) BSE micrographs showing cross section of the reaction layer. Dashed and dotted lines delineate the reaction product morphology zones. Microstructure for two different areas of the $A_{10}Y_{76}Z_{14}$-$C_{10}M_5F_5A_{10}S_{70}$ reaction layer appearance are shown due to the significant variability in the reaction layer.

grains and then a dense layer of mostly cuspidine.

3.5. Analysis of coating material and deposit composition effects

Fig. 10 shows the reaction layer profile, cumulative probability distributions (CPD) for the total reaction layer thickness, and pie charts summarizing representative reaction product phase fractions for each sample. These are grouped based on the RE cation for each $A_{30}RE_{60}Z_{10}$ (Fig. 10 (a-f)) and $A_{10}RE_{76}Z_{14}$ (Fig. 10 (g-l)) sample. Fig. 11 (a-d) shows the reaction depths relative to the initial pellet surface, grouped to compare between CMFAS compositions on the same coating material. Corresponding CPDs are shown for the reaction depth (Fig. 11 (e-h)), overall reaction layer thickness (Fig. 11 (i-l)), and the ratio of the thickness of the reaction layer above-to-below the initial pellet surface (termed 'reaction layer ratio', Fig. 11 (m-p)). Ideally, if the CMFAS exposure produces a thin, uniform reaction layer, the CPDs for reaction depth and thickness will be steep with a low maxima and the CPD for the reaction layer ratio will be high. These figures are used in the following sections to discuss the effects of the coating material and CMFAS composition on the reaction and spreading behavior.

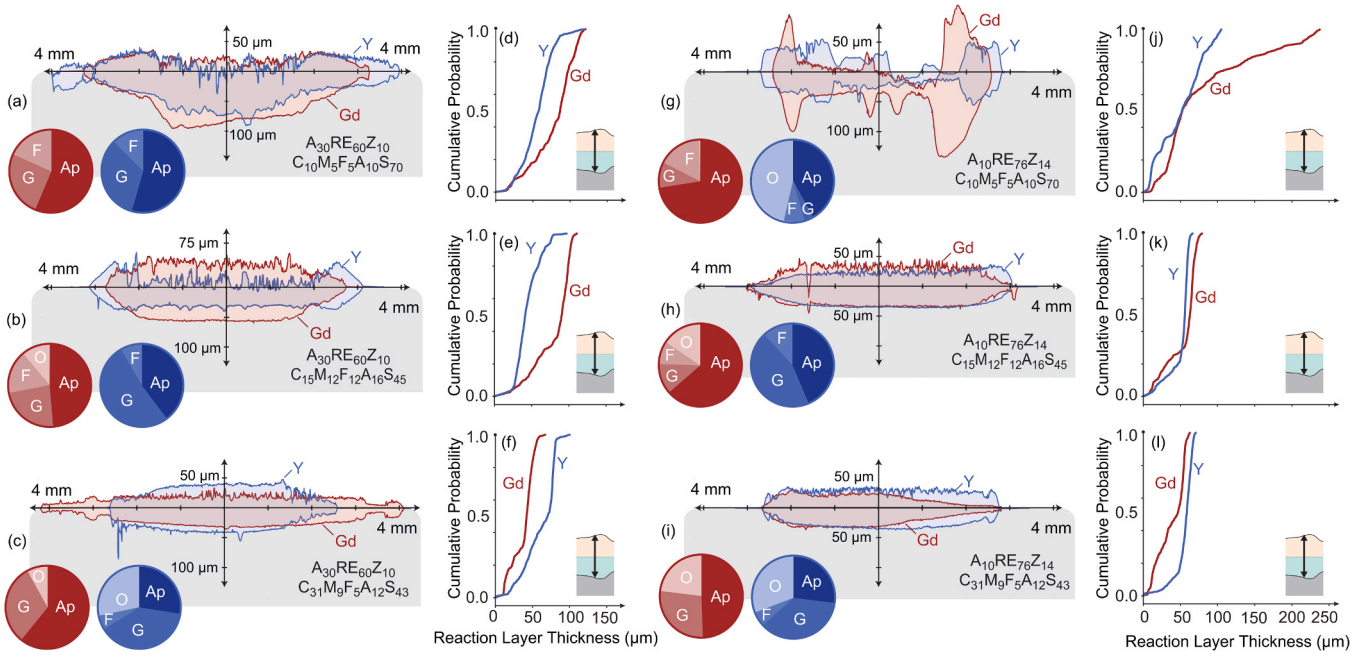

Fig. 10. (a-c, g-i) Reaction layer profiles for each CMFAS exposure test grouped to illustrate the effect of the RE cation identify on the reactions. Pie charts showing volume fractions of key reaction products from representative regions. (d-f, j-l) Cumulative probability distributions of the total reaction layer thicknesses.

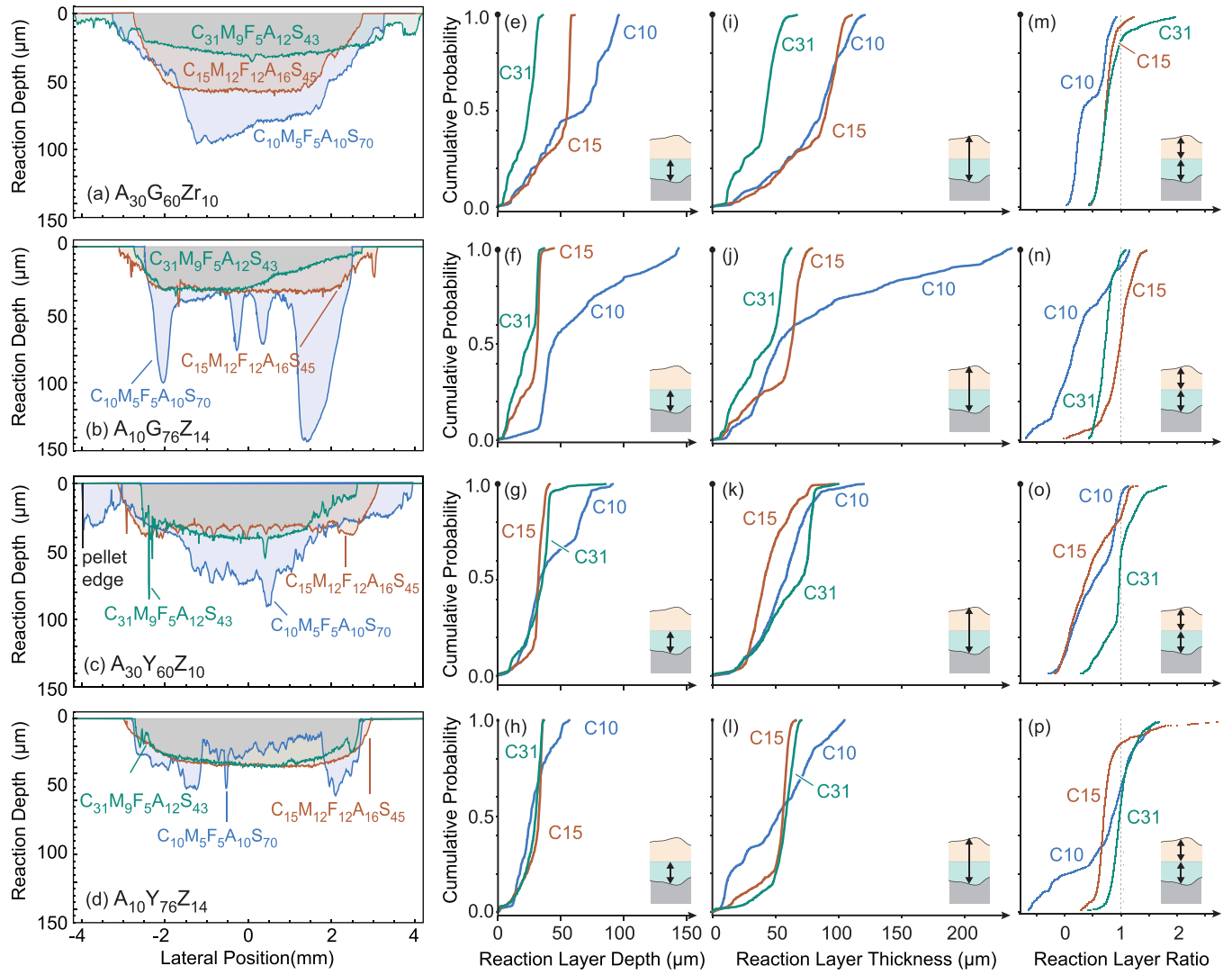

Fig. 11. (a-d) Reaction depth profiles grouped to compare the effect of the CMFAS composition on reactions along with CPDs of the (e-h) the reaction depths, (i-l) total reaction thicknesses, and (m-p) corresponding to tests shown in plot (a-d).

3.5.1. *Influence of RE cation identity*

There is not a single universal feature or trend differentiating the behavior of the Gd- and Y-based coating materials. However, several observations provide relevant insights for coating design. For the low-Al compositions ($A_{10}RE_{76}Z_{14}$), both the Y and Gd samples show thin, uniform reaction layers with minimal spreading upon reacting with $C_{15}M_{12}F_{12}A_{16}S_{45}$ and $C_{31}M_9F_5A_{12}S_{43}$. Conversely, their reactions with the high-Si $C_{10}M_5F_5A_{10}S_{70}$ deposit produce non-uniform, locally varied reaction layers. The amplitude of the lateral variation in the Gd-based samples is greater, resulting in the long tail toward high reaction layer thickness in Fig. 10 (j). For the high-Al ($A_{30}RE_{60}Z_{10}$) systems, the reaction layers formed by $C_{10}M_5F_5A_{10}S_{70}$ and $C_{15}M_{12}F_{12}A_{16}S_{45}$ are slightly thinner with steeper CPD for the Y- than the Gd-based materials, while the trend is reversed for the reaction with $C_{31}M_9F_5A_{12}S_{43}$. An important observation is that while there are some instances where the reaction layer on the Y-based material extends slightly deeper than for the equivalent test on the Gd-based material, the three deepest reaction layers appear for Gd-based materials.

Perhaps the most significant implication is that the addition of aluminates to Y-based zirconate coating materials increases the capacity for reactive crystallization via garnet and cuspidine formation. Thus, Y-based mixed aluminate-zirconate coatings could reduce the performance difference between Y- and Gd-zirconates that originates in capability for increased apatite formation in the latter [3,7,47,55,56]. This would enable utilization of the lower-cost Y-based materials without significant reduction in performance. A second important implication is that the Gd-based materials may be more susceptible to reactions that produce deep or highly nonuniform reactions when exposed to some CMFAS compositions. This behavior is likely more important when considering applications involving dense coating architectures where deep reactive consumption is undesirable.

3.5.2. *Influence of alumina content in coating material*

Although the high-Al coating materials ($A_{30}RE_{60}Z_{10}$) had on average thicker and deeper reaction layers, the response was more uniform for all three CMFAS compositions. The inference is that the addition of alumina could increase the reaction rate, but the alumina can buffer the apatite-forming reactions via garnet or cuspidine formation. In these cases, although the net reaction thickness is higher, the advantages of uniformity and predictability in reaction layer thickness provide value. In cases where there are thinner reaction layers, less coating material that would exfoliate during thermal cycling. However, if the layer thickness is not uniform, there could be regions which would see a more catastrophic coating cracking. Consequently, coating material design in these systems must balance the desirable increase in reaction uniformity and undesirable increase in reaction depth or volume when choosing

coating materials with a higher alumina content.

3.5.3. Influence of CMFAS composition

The maximum reaction depth (Fig. 11(a-d)) is greatest with the Si-rich $C_{10}M_5F_5A_{10}S_{70}$ deposit, where the reaction depths are of order 100 μm or more. This is significant in part because this depth begins to approach the layer thickness for some T/EBC systems implying that if enough deposit is present, reactions could quickly consume a considerable fraction of the coating, even without infiltration into porosity. The difference in reaction depth between $C_{15}M_{12}F_{12}A_{16}S_{45}$ and $C_{31}M_9F_5A_{12}S_{43}$ is most evident for the tests on $A_{30}G_{60}Z_{10}$, while the difference between these two deposits is small for the tests on the Y-based materials. This is contrary to the observations for $Y_2Si_2O_7$ and Y_2SiO_5 [30,31] where coating material reaction layer thickness was smallest (and quite uniform) for the $C_{10}M_5F_5A_{10}S_{70}$ deposit and increased in thickness as the Ca:Si ratio in the CMFAS increased.

The $A_{10}Y_{76}Z_{14}$ coating material produced reaction depths for all three deposits that are most uniform shown by their nearly coincident reaction depth CPDs plots. This material also shows the lowest reaction depth and generally high reaction product ratios against all three CMFAS deposits. Even though exposure to the SiO_2 rich $C_{10}M_5F_5A_{10}S_{70}$ deposit results in some reaction layer depth variations, the fact that this layer is thinner than the layer formed on any other material is a critical distinction between the coating compositions since the resultant stress state in the coating is a function of the overall reaction layer profile.

3.5.4. Influence of coating material microstructure

This study focused primarily on changes in the composition of the candidate coating materials and deposits, while minimizing variations in microstructure between the samples. Thus, the results do not provide direct evidence about how the relative fractions and distribution of individual phases, the fraction and morphology of porosity, and the surface microstructure would influence the spreading, reaction, and infiltration processes. However, the results do provide context to understand how these features, which are each relevant to actual coatings, would change the behavior. First, the apparent speed of reactions with these materials at 1400°C means that any surface structure (e.g., column tips or roughness) would be rapidly dissolved, and the subsequent spreading would converge toward the behavior determined by the reactive wetting characteristics. Second, the results show that in some cases one phase present in the materials is less reactive, e.g. modest shifts in the fluorite compositions, or aluminates that are minimally reacted deeper in some reaction layers. The implication is that fine grain sizes and uniform phase distribution could help avoid spatial variations in the reaction behavior. Future work is needed to confirm these points, and to understand the ability of reactions to block infiltration in highly porous coatings.

4. Conclusions

This work assessed the potential of four novel multiphase coating compositions based on RE-rich zirconates and aluminates for their potential to promote the formation of thin, uniform reaction layers upon reaction with CMFAS to control the thermal stresses that develop during thermal cycling. The reaction layers formed after exposure to three model deposit compositions were analyzed to determine the reaction product constitution and reaction layer morphology and uniformity. Important conclusions include:

1. Increasing the $AlO_{1.5}$ content in the coating material increased the diversity of reaction products, resulting in alternative reaction pathways to promote CMFAS melt consumption besides apatite crystallization.
2. Although in many cases the Y- and Gd-based systems showed similar macroscopic reaction response, i.e. overall depth and reaction layer thickness, to the same CMFAS melts, the reactions with the Gd-based materials involved significant apatite formation while the reactions with the Y-based materials involved more formation of the aluminosilicate garnet and cuspidine phases.
3. Coating materials containing more $AlO_{1.5}$ showed more consistent, uniform reaction layers against all three CMFAS compositions, and for the $AlO_{1.5}$-lean materials, the response of the Y-based materials was more consistent than between the Gd-based materials between the three CMFAS compositions
4. The approach to analyze the entire CMFAS reaction zone when evaluating new candidate coating materials to characterize reaction depth, CMFAS melt spread, reaction product identities and grain morphologies provided unique insights into their CMFAS reaction behavior and potential CMFAS resistance of the coatings.

Declaration of Competing Interest

The authors declare that they have no known competing financial interests or personal relationships that could have appeared to influence the work reported in this paper.

Acknowledgments

This research was supported by NASA award number 80NSSC21C0071 monitored by Dr. Cameron Bodenschatz, in collaboration with QuesTek Innovations LLC. N.H. was supported by the NSF REU program under Award Number DMR-1852044 and through the University of Minnesota MRSEC under Award Number DMR-2011401. Part of this work was carried out in the Characterization Facility at the University of Minnesota, which receives partial support from the NSF through the MRSEC (DMR-2011401) and the NNCI (ECCS-2025124) programs. The sponsors were not involved in the detailed study design, or the data collection, analysis, or interpretation. The authors are grateful to Drs. Noriaki Arai, Pin Lu, and Jiadong Gong (QuesTek Innovations LLC) for the insightful discussions.

References

[1] F.H. Stott, D.J. de Wet, R. Taylor, Degradation of thermal-barrier coatings at very high temperatures, MRS Bull. 19 (1994) 46–49, https://doi.org/10.1557/S0883769400048223.
[2] M.P. Borom, C.A. Johnson, L.A. Peluso, Role of environmental deposits and operating surface temperature in spallation of air plasma sprayed thermal barrier coatings, Surf. Coat. Technol. (1996), https://doi.org/10.1016/S0257-8972(96)02994-5.
[3] D.L. Poerschke, R.W. Jackson, C.G. Levi, Silicate deposit degradation of engineered coatings in gas turbines: progress toward models and materials solutions, Annu Rev. Mater. Res. 47 (2017) 297–330, https://doi.org/10.1146/annurev-matsci-010917-105000.
[4] D.R. Clarke, C.G. Levi, Materials design for the next generation thermal barrier coatings, Annu Rev. Mater. Res. 33 (2003) 383–417, https://doi.org/10.1146/annurev.matsci.33.011403.113718.
[5] C.G. Levi, J.W. Hutchinson, M.-H. Vidal-Sétif, C.A. Johnson, Environmental degradation of thermal-barrier coatings by molten deposits, MRS Bull. 37 (2012) 932–941, https://doi.org/10.1557/mrs.2012.230.
[6] R.W. Jackson, E.M. Zaleski, B.T. Hazel, M.R. Begley, C.G. Levi, Response of molten silicate infiltrated $Gd_2Zr_2O_7$ thermal barrier coatings to temperature gradients, Acta Mater. 132 (2017) 538–549, https://doi.org/10.1016/j.actamat.2017.03.081.
[7] D.L. Poerschke, Developments in thermodynamic models of deposit-induced corrosion of high-temperature coatings, JOM 74 (2022) 260–273, https://doi.org/10.1007/s11837-021-04989-0.
[8] R.W. Jackson, E.M. Zaleski, D.L. Poerschke, B.T. Hazel, M.R. Begley, C.G. Levi, Interaction of molten silicates with thermal barrier coatings under temperature gradients, Acta Mater. (2015), https://doi.org/10.1016/j.actamat.2015.01.038.
[9] C.G. Levi, J.W. Hutchinson, M.H. Vidal-Sétif, C.A. Johnson, Environmental degradation of thermal-barrier coatings by molten deposits, MRS Bull. (2012), https://doi.org/10.1557/mrs.2012.230.
[10] S. Krämer, S. Faulhaber, M. Chambers, D.R. Clarke, C.G. Levi, J.W. Hutchinson, et al., Mechanisms of cracking and delamination within thick thermal barrier systems in aero-engines subject to calcium-magnesium-alumino-silicate (CMAS) penetration, Mater. Sci. Eng. A 490 (2008) 26–35, https://doi.org/10.1016/j.msea.2008.01.006.
[11] W.D. Summers, D.L. Poerschke, M.R. Begley, C.G. Levi, F.W. Zok, A computational modeling framework for reaction and failure of environmental barrier coatings under silicate deposits, J. Am. Ceram. Soc. 103 (2020) 5196–5213, https://doi.org/10.1111/jace.17187.

[12] B.T. Richards, S. Sehr, F. De Franqueville, M.R. Begley, H.N.G. Wadley, Fracture mechanisms of ytterbium monosilicate environmental barrier coatings during cyclic thermal exposure, Acta Mater. 103 (2016) 448–460, https://doi.org/10.1016/j.actamat.2015.10.019.

[13] S. Yang, W. Song, Y. Lavallee, X. Zhou, D.B. Dingwell, H. Guo, Dynamic spreading of re-melted volcanic ash bead on thermal barrier coatings, Corros. Sci. 170 (2020), 108659, https://doi.org/10.1016/j.corsci.2020.108659.

[14] S.J. Yang, W.J. Song, D.B. Dingwell, J. He, H.B. Guo, Surface roughness affects metastable non-wetting behavior of silicate melts on thermal barrier coatings, Rare Met. 41 (2022) 469–481, https://doi.org/10.1007/s12598-021-01773-6.

[15] E.J. Gildersleeve, S. Sampath, Dynamic interactions of ingested molten silicate particles with air plasma sprayed thermal barrier coatings, J. Mater. Res. 35 (2020) 2321–2334, https://doi.org/10.1557/jmr.2020.196.

[16] E. Gildersleeve, V. Viswanathan, S. Sampath, Molten silicate interactions with plasma sprayed thermal barrier coatings: role of materials and microstructure, J. Eur. Ceram. Soc. 39 (2019) 2122–2131, https://doi.org/10.1016/j.jeurceramsoc.2019.01.023.

[17] B. Zhang, W. Song, H. Guo, Wetting, infiltration and interaction behavior of CMAS towards columnar YSZ coatings deposited by plasma spray physical vapor, J. Eur. Ceram. Soc. 38 (2018) 3564–3572, https://doi.org/10.1016/j.jeurceramsoc.2018.04.013.

[18] S. Krämer, J. Yang, C.G. Levi, C.A. Johnson, Thermochemical interaction of thermal barrier coatings with molten CaO-MgO-Al_2O_3-SiO_2 (CMAS) deposits, J. Am. Ceram. Soc. 89 (2006) 3167–3175, https://doi.org/10.1111/j.1551-2916.2006.01209.x.

[19] Kucuk, A., Clare, A.G., Jones L., Surface tension calculation of glass melts at 1400°C ⟨http://glassproperties.com/surfacetension/⟩.

[20] W. Song, Y. Lavallee, K.U. Hess, U. Kueppers, C. Cimarelli, D.B. Dingwell, Volcanic ash melting under conditions relevant to ash turbine interactions, Nat. Commun. 7 (2016) 1–10, https://doi.org/10.1038/ncomms10795.

[21] W. Song, Z. Major, Y. Guo, S. Karsch, H. Guo, K. Ferenc, et al., Biomimetic super "silicate" phobicity and superhydrophobicity of thermal barrier coating, SSRN Electron J. (2021), https://doi.org/10.2139/ssrn.3997818.

[22] B. Zhang, W. Song, L. Wei, Y. Xiu, H. Xu, D.B. Dingwell, et al., Novel thermal barrier coatings repel and resist molten silicate deposits, Scr. Mater. 163 (2019) 71–76, https://doi.org/10.1016/j.scriptamat.2018.12.028.

[23] A. Nieto, R. Agrawal, L. Bravo, C. Hofmeister-Mock, M. Pepi, A. Ghoshal, Calcia–magnesia–alumina–silicate (CMAS) attack mechanisms and roadmap towards Sandphobic thermal and environmental barrier coatings, Int Mater. Rev. 66 (2021) 451–492, https://doi.org/10.1080/09506608.2020.1824414.

[24] D. Müller, K.U. Hess, U. Kueppers, S. Lokachari, D.B. Dingwell, G. Wolf, et al., Rheological and chemical interaction between volcanic ash and thermal barrier coatings, Surf. Coat. Technol. 412 (2021), 127049, https://doi.org/10.1016/j.surfcoat.2021.127049.

[25] D. Müller, K.U. Hess, U. Kueppers, D.B. Dingwell, Effects of the dissolution of thermal barrier coating materials on the viscosity of remelted volcanic ash, Am. Miner. 105 (2020) 1104–1107, https://doi.org/10.2138/am-2020-7334.

[26] C. Mock, M.J. Walock, A. Ghoshal, M. Murugan, M. Pepi, Adhesion behavior of calcia–magnesia–alumino–silicates on gadolinia-yttria-stabilized zirconia composite thermal barrier coatings, J. Mater. Res. (2020) 1–11, https://doi.org/10.1557/jmr.2020.184.

[27] R. Naraparaju, M. Hüttermann, U. Schulz, P. Mechnich, Tailoring the EB-PVD columnar microstructure to mitigate the infiltration of CMAS in 7YSZ thermal barrier coatings, J. Eur. Ceram. Soc. 37 (2017) 261–270, https://doi.org/10.1016/j.jeurceramsoc.2016.07.027.

[28] D.L. Poerschke, C.G. Levi, Effects of cation substitution and temperature on the interaction between thermal barrier oxides and molten CMAS, J. Eur. Ceram. Soc. 35 (2015) 681–691, https://doi.org/10.1016/j.jeurceramsoc.2014.09.006.

[29] W. Song, Y. Lavallée, F.B. Wadsworth, K.U. Hess, D.B. Dingwell, Wetting and spreading of molten volcanic ash in jet engines, J. Phys. Chem. Lett. 8 (2017) 1878–1884, https://doi.org/10.1021/acs.jpclett.7b00417.

[30] W.D. Summers, D.L. Poerschke, A.A. Taylor, A.R. Ericks, C.G. Levi, F.W. Zok, Reactions of molten silicate deposits with yttrium monosilicate, J. Am. Ceram. Soc. (2019) 2919–2932, https://doi.org/10.1111/jace.16972.

[31] W.D. Summers, D.L. Poerschke, D. Park, J.H. Shaw, F.W. Zok, C.G. Levi, Roles of composition and temperature in silicate deposit-induced recession of yttrium disilicate, Acta Mater. 160 (2018) 34–46, https://doi.org/10.1016/j.actamat.2018.08.043.

[32] M.P. Schmitt, S.P. Stepanoff, A.K. Rai, P.E. Lauer, R.W. Spangler, D.E. Wolfe, Enhanced calcium–magnesium–aluminosilicate (CMAS) resistance of $GdAlO_3$ (GAP) for composite thermal barrier coatings, J. Am. Ceram. Soc. 105 (2022) 4435–4448, https://doi.org/10.1111/jace.18408.

[33] L.R. Turcer, A.R. Krause, H.F. Garces, L. Zhang, N.P. Padture, Environmental-barrier coating ceramics for resistance against attack by molten calcia-magnesia-aluminosilicate (CMAS) glass: part I, $YAlO_3$ and γ-$Y_2Si_2O_7$, J. Eur. Ceram. Soc. 38 (2018) 3905–3913, https://doi.org/10.1016/j.jeurceramsoc.2018.03.021.

[34] M. Fritsch, H. Klemm, M. Herrmann, B. Schenk, Corrosion of selected ceramic materials in hot gas environment, J. Eur. Ceram. Soc. 26 (2006) 3557–3565, https://doi.org/10.1016/j.jeurceramsoc.2006.01.015.

[35] Z. Xue, Y. Ma, S. Gong, H. Guo, Impermeability of $Y_3Al_5O_{12}$ ceramic against molten glassy calcium-magnesium-alumina-silicate, Chin. J. Aeronaut. 31 (2018) 2306–2311, https://doi.org/10.1016/j.cja.2018.02.007.

[36] S. Sun, Z. Xue, W. He, J. He, Q. Li, H. Guo, Corrosion resistant plasma sprayed $(Y_{0.8}Gd_{0.2})_3Al_5O_{12}$/YSZ thermal barrier coatings towards molten calcium-magnesium-alumina-silicate, Ceram. Int. 45 (2019) 8138–8144, https://doi.org/10.1016/j.ceramint.2019.01.114.

[37] H. Yamane, K. Ogawara, M. Omori, T. Hirai, Thermal expansion and athermal phase transition of $Y_4Al_2O_9$ ceramics, J. Am. Ceram. Soc. 78 (1995) 1230–1232, https://doi.org/10.1111/j.1151-2916.1995.tb08474.x.

[38] C.M. Weyant, K.T. Faber, Processing-microstructure relationships for plasma-sprayed yttrium aluminum garnet, Surf. Coat. Technol. 202 (2008) 6081–6089, https://doi.org/10.1016/j.surfcoat.2008.07.008.

[39] D.L. Poerschke, J.S. Van Sluytman, K.B. Wong, C.G. Levi, Thermochemical compatibility of ytterbia-(hafnia/silica) multilayers for environmental barrier coatings, Acta Mater. 61 (2013) 6743–6755, https://doi.org/10.1016/j.actamat.2013.07.047.

[40] D.L. Poerschke, D.D. Hass, S. Eustis, G.G.E. Seward, J.S. Van Sluytman, C.G. Levi, Stability and CMAS resistance of ytterbium-silicate/hafnate EBCs/TBC for SiC composites, J. Am. Ceram. Soc. 98 (2015) 278–286, https://doi.org/10.1111/jace.13262.

[41] Y.-C. Yu, D.L. Poerschke, Design of thermal and environmental barrier coatings for Nb-based alloys for high-temperature operation, Surf. Coat. Technol. 431 (2022), 128007, https://doi.org/10.1016/j.surfcoat.2021.128007.

[42] M.P. Schmitt, J.L. Stokes, A.K. Rai, A.J. Schwartz, D.E. Wolfe, Durable aluminate toughened zirconate composite thermal barrier coating (TBC) materials for high temperature operation, J. Am. Ceram. Soc. 102 (2019) 4781–4793, https://doi.org/10.1111/jace.16317.

[43] Y. Yu, E.P. Godbole, J. Berrios, N. Hewage, D.L. Poerschke, Slow sintering in garnet-containing Y and Gd zirconate – aluminate mixtures for thermal barrier coatings, J. Am. Ceram. Soc. 106 (2023), https://doi.org/10.1111/jace.19121.

[44] E.P. Godbole, N. Hewage, A. von der Handt, D.L. Poerschke, Quantifying efficiency of reactions between CMAS melts and rare earth aluminate zirconate thermal and environmental barrier coating materials, J. Eur. Cer Soc. (2023), https://doi.org/10.1016/j.jeurceramsoc.2023.05.009.

[45] A.S. Chikhalikar, E.P. Godbole, D.L. Poerschke, Stability of oxide-sulfate mixtures and implications for deposit-induced degradation of advanced alloys and coatings, Acta Mater. 237 (2022), 118184, https://doi.org/10.1016/j.actamat.2022.118184.

[46] E. Godbole, N. Karthikeyan, D. Poerschke, Garnet stability in the Al–Ca–Mg–Si–Y–O system with implications for reactions between TBCs, EBCs, and silicate deposits, J. Am. Ceram. Soc. 103 (2020) 5270–5282, https://doi.org/10.1111/jace.17176.

[47] E. Godbole, A. von der Handt, D. Poerschke, Apatite and garnet stability in the Al–Ca–Mg–Si–(Gd/Y/Yb)–O systems and implications for T/EBC: CMAS reactions, J. Am. Ceram. Soc. 105 (2022) 1596–1609, https://doi.org/10.1111/jace.18179.

[48] D.L. Poerschke, G.G.E. Seward, C.G. Levi, Influence of Yb:Hf ratio on ytterbium hafnate/molten silicate (CMAS) Reactivity, J. Am. Ceram. Soc. 99 (2016) 651–659, https://doi.org/10.1111/jace.13964.

[49] D.L. Poerschke, T.L. Barth, C.G. Levi, Equilibrium relationships between thermal barrier oxides and silicate melts, Acta Mater. 120 (2016) 302–314, https://doi.org/10.1016/j.actamat.2016.08.077.

[50] H. Yamane, M. Omori, A. Okubo, T. Hirai, High-temperature phase transition of $Y_4Al_2O_9$, J. Am. Ceram. Soc. 76 (1993) 2382–2384, https://doi.org/10.1111/j.1151-2916.1993.tb07783.x.

[51] D.L. Poerschke, T.L. Barth, O. Fabrichnaya, C.G. Levi, Phase equilibria and crystal chemistry in the calcia-silica-yttria system, J. Eur. Ceram. Soc. 36 (2016) 1743–1754, https://doi.org/10.1016/j.jeurceramsoc.2016.01.046.

[52] U. Kolitsch, H.J. Seifert, F. Aldinger, Phase relationships in the systems RE_2O_3-Al_2O_3-SiO_2 (RE = rare earth element, Y, and Sc), J. Phase Equilib. 19 (1998) 426–433, https://doi.org/10.1361/105497198770341905.

[53] U. Kolitsch, H.J. Seifert, F. Aldinger, Phase relationships in the system Gd_2O_3-Al_2O_3-SiO_2, J. Alloy. Compd. 257 (1997) 104–114, https://doi.org/10.1016/S0925-8388(96)03121-0.

[54] U. Kolitsch, H.J. Seifert, T. Ludwig, F. Aldinger, Phase equilibria and crystal chemistry in the Y_2O_3–$Al_2O_3SiO_2$ system, J. Mater. Res. 14 (1999) 447–455, https://doi.org/10.1557/JMR.1999.0064.

[55] S. Krämer, J. Yang, C.G. Levi, Infiltration-inhibiting reaction of gadolinium zirconate thermal barrier coatings with CMAS melts, J. Am. Ceram. Soc. 91 (2008) 576–583, https://doi.org/10.1111/j.1551-2916.2007.02175.x.

[56] J.M. Drexler, C.H. Chen, A.D. Gledhill, K. Shinoda, S. Sampath, N.P. Padture, Plasma sprayed gadolinium zirconate thermal barrier coatings that are resistant to damage by molten Ca-Mg-Al-silicate glass, Surf. Coat. Technol. 206 (2012) 3911–3916, https://doi.org/10.1016/j.surfcoat.2012.03.051.